Numerical Study on the Retrofitting of Exterior RC Beam-column Joints with CFRP Composites Using the Grooving Method

Issam Bouroumana[1*], Zahreddine Nafa[1], Ghania Nigri[1]

[1] Laboratory of Civil Engineering and Hydraulics (LGCH), Faculty of Science and Technology, University of 8 Mai 1945 Guelma, 24000 Guelma, P.O.B. 401, Algeria
[*] Corresponding author, e-mail: bouroumana.issam@univ-guelma.dz

Abstract

Retrofitting seismically deficient beam-column joints (BCJs) in reinforced concrete (RC) structures is crucial to preventing collapse during high-intensity earthquakes. Fiber reinforced polymer (FRP) composites have proven effective for retrofitting these components, but debonding of the FRP from concrete surfaces remains a challenge. Recently, the grooving method (GM) has emerged as a promising solution to mitigate this issue, enhancing the bond between FRP and concrete. This paper presents a numerical investigation of BCJs retrofitted with FRP composites using the GM, focusing on various design parameters. The study utilized finite element models developed in ABAQUS, incorporating the concrete damage plasticity (CDP) model to simulate the nonlinear behavior of concrete. The interface between the concrete and FRP was modeled as a perfect bond, simulating the strong adhesion provided by the GM. The numerical results were validated against experimental data from two BCJ specimens, showing good agreement in terms of load-displacement behavior, peak loads, and failure modes. Key parameters studied include the beam longitudinal reinforcement ratio, column axial load ratio, and joint aspect ratio. The findings reveal that these parameters significantly affect the shear capacity of retrofitted joints, impacting the efficiency of the retrofitting.

Keywords

FRP, numerical analysis, beam-column joint, grooving method

1 Introduction

The resilience of reinforced concrete (RC) structures in civil engineering depends significantly on the integrity of beam-column joints (BCJs), which are among the most vulnerable and critical components of RC frames, particularly when subjected to seismic events. However, BCJs built before the implementation of modern seismic design codes, especially those with beam flexural capacities exceeding those of the columns, often show seismic deficiencies. These deficiencies include insufficient or a complete lack of transverse reinforcement in the joint region, inadequate anchorage for beam longitudinal reinforcement, and a failure to adhere to the principles of strong column-weak beam design [1]. These deficiencies make the structural elements non-compliant with seismic standards, leaving them vulnerable to joint shear failure due to the high shear stresses in the joint panel during severe earthquakes. This failure typically occurs in a brittle manner, causing severe damage and potentially leading to the collapse of the entire structure [2].

Earthquake-induced damage to concrete structures can be so severe that reconstruction costs become prohibitively high. Therefore, retrofitting these structural components is essential to reduce the risk of severe damage or complete collapse during seismic events.

Over the years, researchers have explored diverse retrofitting methods to enhance the seismic performance of reinforced concrete beam-column joints (RC-BCJs), employing an extensive array of retrofitting materials. One notable approach is the utilization of RC or steel jacketing [3–6], which has been confirmed to enhance the strength, stiffness, ductility, and energy dissipation of RC-BCJs. Additionally, ferrocement jacketing has been applied for retrofitting BCJs using various types of mortar [7, 8].

In recent years, fiber reinforced polymer (FRP) composites have emerged as the preferred choice for seismic retrofitting, surpassing traditional materials due to their exceptional attributes. Externally bonded reinforcement (EBR)

FRP composites, in particular, have gained widespread acceptance owing to their remarkable strength-to-weight ratio, lightweight nature, excellent corrosion resistance, and ease of installation [9]. Experimental studies have extensively validated the efficacy of EBR-FRP composites in reinforcing BCJs vulnerable to seismic forces [10–16]. These studies have explored various FRP sheet configurations bonded to non-seismically designed BCJs, including L-shape, U-shape, X-shape, and T-shape, each tailored to address specific seismic vulnerabilities. For instance, Le-Trung et al. [10] employed T-shape, L-shape, and X-shape configurations to retrofit shear-deficient BCJs, with the X-shaped pattern exhibiting superior strength and ductility compared to T and L-shaped configurations. Similarly, Ghobara and Said [11] investigated the retrofitting of shear-deficient BCJs using U-shape and X-shape configurations. Generally, for shear-deficient joints, the U-, X-, and T-shaped sheet patterns are commonly applied to BCJs [12–14]. Meanwhile, joints with insufficient beam longitudinal reinforcement anchorage often receive L-shaped sheets affixed to the beam's flanges [15, 16]. However, it is important to acknowledge a significant drawback of the EBR-FRP composite technique, namely, the risk of debonding of FRP sheets from concrete surfaces, which emerges as a prevalent failure mode in many retrofitted BCJs. Consequently, while EBR-FRP composites offer substantial improvements in the seismic performance of deficient BCJs in terms of strength, ductility, and energy dissipation capacity, strategies to mitigate debonding are crucial for ensuring the long-term effectiveness of retrofit measures.

In response to the challenge of debonding FRP sheets, researchers have proposed new techniques to mitigate this issue. One effective method is the anchorage of FRP composites on the surfaces of the joint area in BCJs, which helps prevent or delay undesired debonding failure. Various anchorage methods have been proposed to ensure the FRP remains bonded, including transverse wrapping with FRP strips on the beam, mechanical anchorage, bolted steel plates, steel angles, bonding concrete covers with CFRP wrapping, and using self-tapping screws for FRP strips [17]. The near-surface mounted (NSM) technique, which involves embedding FRP strips or bars in grooves, is another effective method for enhancing the performance of BCJs against debonding failure [1, 18]. Furthermore, surface preparation plays a critical role in ensuring a strong adhesive bond with the substrate. Proper surface preparation techniques, such as grinding, sandblasting, and water jetting, are essential for improving adhesion and reducing the risk of debonding [19].

In recent few years, the grooving method (GM), introduced to prevent or delay premature debonding failure. This technique involves creating grooves or indentations on the concrete surface before applying the FRP sheets. In a notable study by Mostofinejad and Akhlaghi [20], the effectiveness of GM in seismic retrofitting of shear-deficient BCJs was investigated. The study examined various configurations of FRP sheets combined with FRP fan anchors. Results demonstrated the complete elimination of debonding events. Additionally, Mostofinejad and Hajrasouliha [19, 21] studied the FRP-retrofitting of 3D corner deficient joint using GM to delay the debonding of FRP sheets from the concrete substrate. Their results showed that the brittle shear failure mode in joint area changed into a flexural one in the beam. In another investigation, Ilia and Mostofinejad [22] tested five half-scale exterior BCJ retrofitted with GM combined with FRP anchorage system, the tested joints were strong in beams and weak in columns. The results showed a significant enhancement in strength, ductility an energy dissipation with relocating the plastic hinge away from the joint area. Further, Ilia et al. [23] experimentally assessed GM's efficacy for deficient BCJs, considering different FRP sheet configurations and anchoring methods. Across all tested retrofitting configurations, an improvement of up to 80% in strength capacity was observed, with the plastic hinges relocated into the beam. Moreover, Davodikia et al. [24] conducted a comparative study on the effectiveness of conventional surface preparation versus the GM in seismic retrofitting of BCJs. Four BCJ specimens were experimentally tested to evaluate the performance of both techniques. The same FRP configurations were applied in both cases. The study revealed that the GM resulted in a stronger adhesion between the FRP layer and the concrete substrate compared to conventional surface preparation, thereby eliminating the separation phenomenon in the joint panel.

The retrofitting of RC-BCJs using carbon fiber reinforced polymer (CFRP) composites has shown promise, particularly through the GM. However, a comprehensive understanding of how various key parameters influence the performance of these retrofitted joints remains limited. The GM offers significant potential for improving bond strength and overall joint performance, yet existing studies often focus on individual parameters or alternative retrofitting techniques. Furthermore, there is a lack of extensive validation of numerical models, such as those using

the concrete damage plasticity (CDP) model in ABAQUS, against experimental results for GM-retrofitted joints.

To address these gaps, this study investigates the performance of RC-BCJs retrofitted with CFRP composites via the GM under various parameters. The study employs numerical models developed using the finite element (FE) software ABAQUS. The numerical findings are verified against test results of two BCJ specimens in terms of load-displacement curves, peak loads, and failure modes. The CDP model implemented in ABAQUS is used to simulate the behavior of the concrete material. Due to the strong bond strength properties resulting from the GM between the CFRP composite and the concrete substrate, a perfect bond simulation is employed to ensure no bond slip occurs during analysis. The key parameters in the numerical study include the flexural reinforcement ratio of the beam, column axial load ratio, joint aspect ratio, and joint transverse reinforcement. The effects of these key parameters on the joint shear capacity, load-displacement response, and damage index are thoroughly investigated in the parametric study.

2 Summary of experimental test

To rigorously validate the accuracy of the numerical models, two exterior RC-BCJ specimens, namely NS and R2NS, were selected from a recently published study [24]. The NS specimen underwent testing without any retrofitting (control). As displayed in Fig. 1, The NS specimen was intentionally designed without transverse reinforcement in
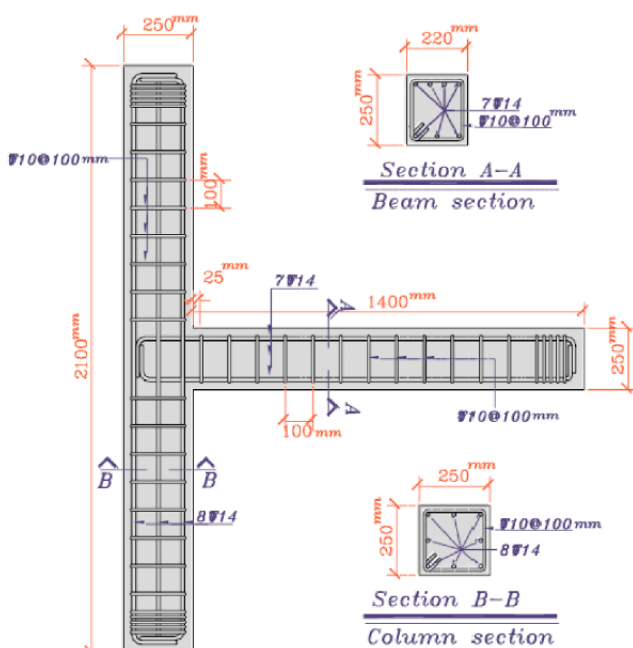

Fig. 1 NS and R2NS BCJ specimens – dimensions and reinforcement details [24]

the joint panel, and with an increased spacing of stirrups in both the beam and columns. This intentional design aimed to create insufficient shear strength in the joint panel, simulating the conditions of an aged non-seismic RC-BCJ. The R2NS specimen was also non-seismic joint. It was tested after being reinforced with CFRP sheets in different configurations. Including:

1. two U-shaped sheets were placed in the joint panel with the fiber's direction parallel to the axis of the beam;
2. two layers of sheets were installed on both sides of the column with the fiber's direction parallel to the axis of the column;
3. finally, two wrapping layers were placed around the beam end, and the two-column ends respectively.

The CFRP layers were affixed to the concrete substrate using a GM. the retrofitted specimen details are illustrated in Fig. 2. In both sub-assemblages, the column's cross-sectional dimensions were 250 × 250 mm, with a height of 2100 mm. additionally, the beam had a cross-sectional dimension of 220 × 250 mm, extending 1400 mm from the column face. Fig. 1 displays the reinforcement and the detailed dimensions of the two selected BCJs.

The NS and R2NS sub-assemblies both experienced a constant axial load of 175 KN applied at the top of the column. This load corresponds to 0.1 times $f_c' \times A_g$, where f_c' represents the compressive strength of the concrete, and A_g denotes the cross-sectional dimensions of the column. Following the axial load, cyclic lateral displacements were applied to the beam tip in two opposite directions. The lateral load history consisted of several sets of three cycles. Each set featured varying amplitudes of horizontal displacement, with these amplitudes remaining constant within each set. However, these amplitudes progressively increased across consecutive sets of cycles.

For a more detailed account of the experimental procedures and results, we kindly refer readers to the study published by Davodikia et al [24].

3 Finite element modelling

The utilization of FE modelling for the study of concrete structural members behaviour presents an efficient and cost-effective approach when compared to the typically time-consuming and expensive laboratory testing methods [25]. Thus, the FE code ABAQUS software is employed in this research to accurately simulate the complex nonlinear characteristics of concrete structures, thanks to its extensive material and element library.

(a)

(b)
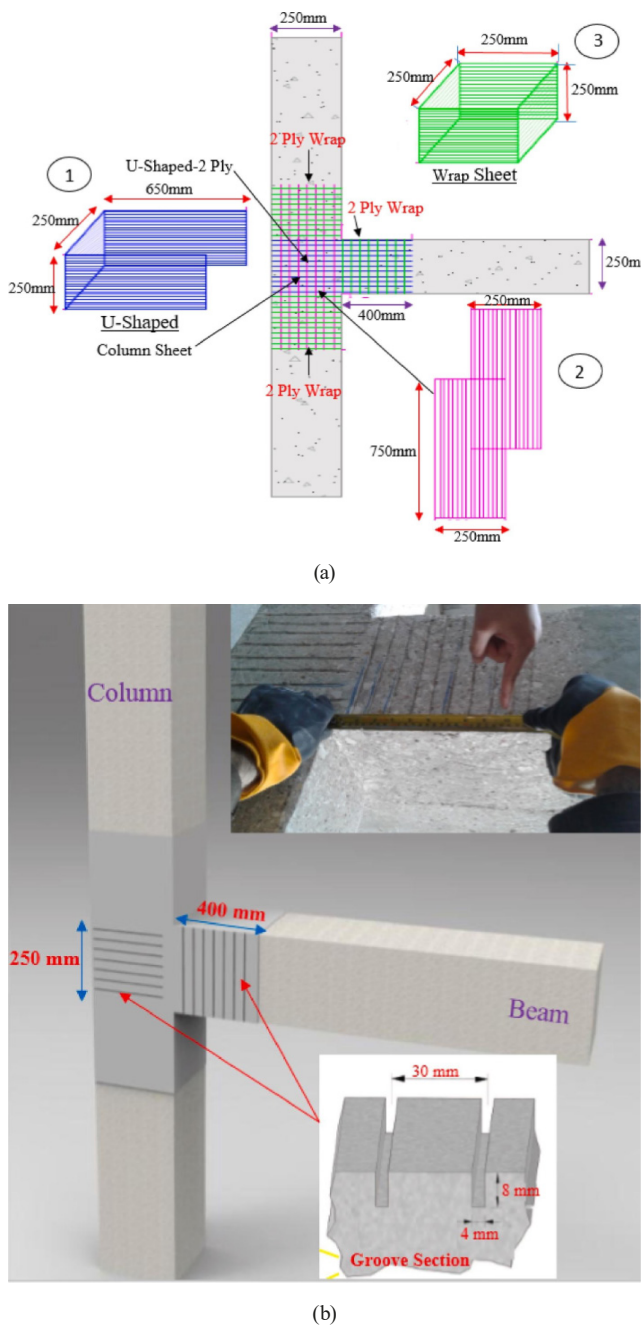
Fig. 2 Retrofitting details of R2NS specimen; (a) Layers configurations detail; (b) Grooving method detail [24]

The quasi-static analysis using ABAQUS/Explicit was used instead of the static analysis approach to overcome the numerical convergence issues that often arise during the simulation of cracked concrete using static analysis method [25]. However, the explicit analysis is commonly employed for dynamics problems, but it can be effectively applied to static solutions involving a slow rate of loading [26]. An essential criterion for ensuring an appropriate loading rate is to keep the kinetic energy of the entire model significantly lower than the internal energy

throughout the analysis. In this study, the selection of the loading rate, defined as the ratio of applied displacement to the loading time (step time), was investigated across various velocities. Notably, the loading rate depends solely on the loading time when the applied displacement is specified. By monitoring the model's kinetic energy, it was determined that a loading rate of 9.5 mm/s yielded accurate results compared to experimental ones. Additionally, a smooth step amplitude was utilized to mitigate internal effects generated by the kinetic energy.

The following sections provided a succinct overview detailing the methodology utilized in constructing the FE model.

3.1 Element types, interactions and meshing

The model's geometrical characteristics were maintained in similarity to those of the test specimens. A four-node linear tetrahedron (C3D4) elements were used for concrete part and the loading steel plate. Two-node linear 3D truss elements (T3D2) were used to model steel reinforcements. A four node (S4R) shell element was used to simulate the CFRP composites. The steel reinforcements were considered embedded inside the surrounding concrete using embedded constraint in ABAQUS. Based on the robust bond strength resulting from the GM between CFRP composites and the concrete substrate, it is presumed that the interactions between the CFRP layers and the underlying concrete substrate yield a perfect bond. A 45 mm thick steel plate was used to apply the load in the beam tip. The interaction between the loading plate and the concrete substrate was also modelled using a perfect bond. After conducting mesh sensitivity analysis, an approximate global mesh size of 50 mm was selected for concrete part and steel reinforcement, with 25 mm approximate global mesh size chosen for CFRP material.

3.2 Concrete modelling

In the ABAQUS software, a range of models is available to capture the nonlinear behaviour of concrete. In this current study, our simulation relies on the CDP model to replicate concrete's behaviour, which has demonstrated its efficacy in modelling concrete behaviour based on multiple prior investigations [27, 28]. The CDP model is categorized as a continuum, plasticity-based, and damage model [29]. It incorporates the primary failure modes, encompassing the development of tensile cracks and the compressive crushing of concrete material [29]. Additionally, the model considers the degradation of elastic stiffness by

incorporating two damage variables in compression and tension, denoted as d_c and d_t respectively, as illustrated in Fig. 3 [30]. These variables can range from zero, representing an undamaged material, to one, signifying complete strength loss. It is worth noting that the CDP model necessitates specific material definitions, encompassing:

1. Plasticity parameters;
2. Uniaxial stress-strain relationship under compression and tension;
3. Damage scalar parameters d_c and d_t under compression and tension respectively.

In order to effectively model concrete behavior, it is essential to take into account four specific plasticity parameters outlined in the CDP model. These parameters, have been succinctly summarized in Table 1. Among them, the dilation angle plays a critical role in influencing the accuracy of the results. This value significantly affects the material's volumetric response under compression, making its proper calibration crucial for achieving realistic simulation outcomes. The recommended range for the
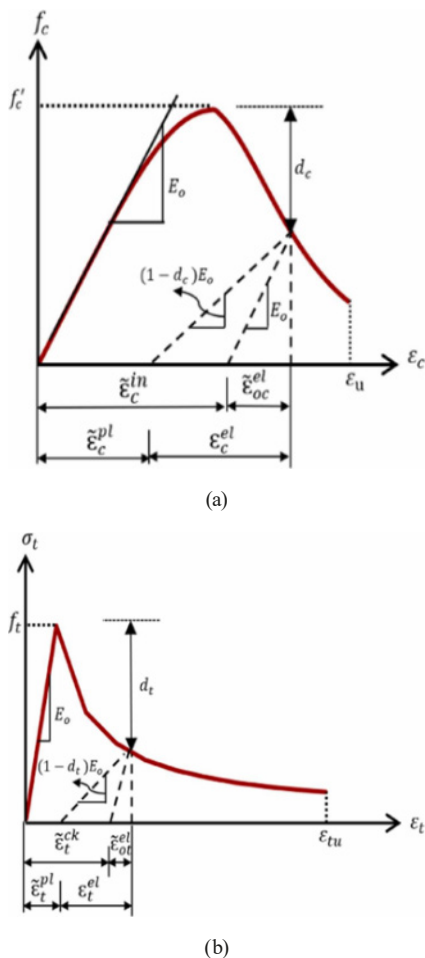
Table 1 Plasticity parameters of CDP model

Parameter name	Value
Dilation angle	40
Eccentricity	0.1
Ratio of biaxial to uniaxial compressive strength	1.16
The ratio of second stress invariant on the tensile meridian	0.667

dilation angle is 31° to 42° [31]. To evaluate the impact of different dilation angles on analysis accuracy, values of 36°, 38°, 40°, and 42° were assessed using the model for the NS specimen. Fig. 4 shows the analysis results for the examined dilation angles in comparison with experimental results. The results are highly dependent on the dilation angle value. The peak load increased with the magnitude of the dilation angle. As shown in Fig. 4, a value of 40° can reasonably capture the experimental load-displacement curve among others. Therefore, the dilation angle was set to 40° for all subsequent analyses.

To characterize the stress-strain behaviour of concrete under compression in our research, we have utilized the model introduced by Saenz [32]. The equations governing the presumed compressive stress-strain relationship, as per the Saenz model, can be found in Eqs. (1)–(6). The concrete's ultimate strain ε_f was deliberately set at a large value of 0.035 to mitigate potential numerical difficulties [26]. The young's modulus of concrete, E_c was calculated by ACI 318-19 [33] as depicted in Eq. (7), and the Poisson's ratio was assumed to be 0.2.

$$\sigma_C = \frac{E_C \times \varepsilon_C}{1+\left(R+R_E-2\right)\left(\dfrac{\varepsilon_c}{\varepsilon_0}\right)-\left(2R-1\right)\left(\dfrac{\varepsilon_c}{\varepsilon_0}\right)^2+R\left(\dfrac{\varepsilon_c}{\varepsilon_0}\right)^3} \quad (1)$$

(a)

(b)

Fig. 3 Concrete material definition; (a) In compression; (b) In tension [30]
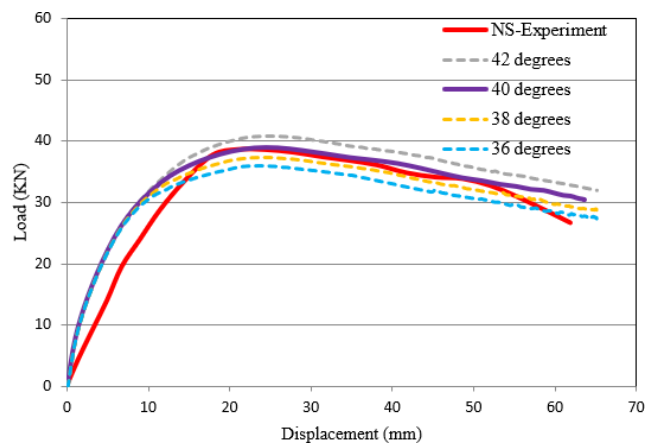

Fig. 4 Load-displacement response of NS model with varying dilation angles

$$R = \frac{R_E(R_\sigma - 1)}{(R_\varepsilon - 1)^2} - \left(\frac{1}{R_\varepsilon}\right) \tag{2}$$

$$R_E = \frac{E_c}{E_0} \tag{3}$$

$$R_\sigma = \frac{f_c'}{\sigma_f} \tag{4}$$

$$R_\varepsilon = \frac{\varepsilon_f}{\varepsilon_0} \tag{5}$$

$$E_0 = \frac{f_c'}{\varepsilon_0} \tag{6}$$

$$E_c = 4700\sqrt{f_c'} \tag{7}$$

In Eqs. (1)–(7):
- σ_c: concrete's compressive stress (MPa);
- E_c: Young's modulus of concrete (MPa);
- E_0: secant modulus of concrete (MPa);
- f_c': compressive strength of concrete (MPa);
- ε_c: compressive strain of concrete;
- ε_0: strain corresponding to f_c';
- ε_f: maximum concrete compressive strain;
- σ_f: concrete's compressive stress at maximum strain (MPa);
- R: ratio relation;
- R_E: modular ratio;
- R_σ: stress ratio;
- R_ε: strain ratio.

In the CDP model, the compression-induced stress-strain relationship of concrete is incorporated by introducing an inelastic strain component denoted as $\varepsilon_c^{\sim in}$ as depicted in Eq. (8), this inelastic strain is equivalent to the total strain minus the elastic strain.

$$\varepsilon_c^{\sim in} = \varepsilon_c - \varepsilon_{0c}^{\sim el}, \quad \varepsilon_{0c}^{\sim el} = \frac{\sigma_c}{E_c} \tag{8}$$

The scalar damage parameter in compression, referred to as d_c, is a key component of the model and is incorporated solely within the descending branch of the stress-strain curve, as outlined in Eq. (9), based on Jankowiak and Łodygowski [34].

$$d_t = 1 - \frac{\sigma_c}{f_c'} \tag{9}$$

To ensure accurate concrete material representation, it is essential to refer to Fig. 5, which provides critical data for model definition. Fig. 5(a) illustrates the relationship between compressive stress and inelastic strain, while Fig. 5(b) presents the correlation between the compression damage parameter and inelastic strains. This comprehensive representation aids in accurately defining the concrete material behaviour under compression within the CDP model.

Moreover, fracture energy criteria were employed to model the tensile behaviour of concrete, utilizing the stress-crack width displacement response based on Hillerborg et al. [35], as depicted in Fig. 6. Here, f_t represents the tensile strength of concrete, computed in accordance with ACI 318-19 [33], as outlined in Eq. (10). The parameter G_f denotes the fracture energy, which signifies the energy required to generate a unit area of crack surface and is illustrated by the area under the tensile stress-crack width displacement curve. The fracture
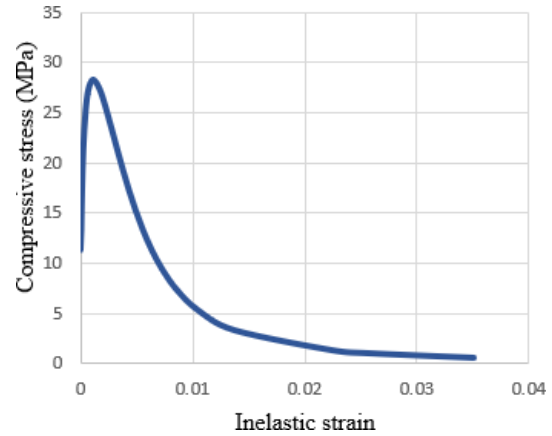
(a)
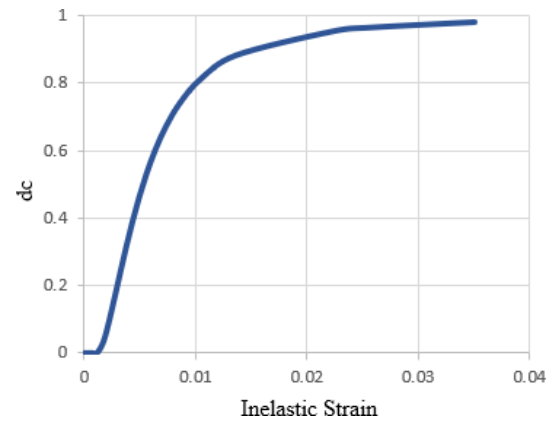
(b)

Fig. 5 Definition of concrete compressive behaviour in the CDP model; (a) Compressive stress vs. inelastic strain; (b) Damage parameter vs. inelastic strain
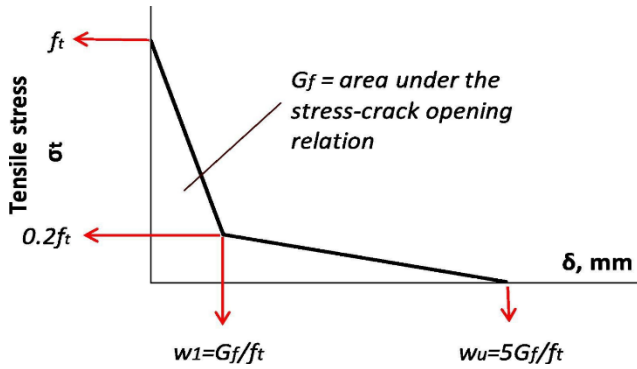
Fig. 6 Relationship between uniaxial tensile stress and crack width in concrete [26]

(a)

(b)

Fig. 7 Definition of tensile behaviour of concrete in the CDP model; (a) Tensile stress vs. tensile displacement; (b) Damage parameter vs. tensile displacement

energy can help to prevent mesh-sensitivity and can be obtained by Eq. (11) [36]:
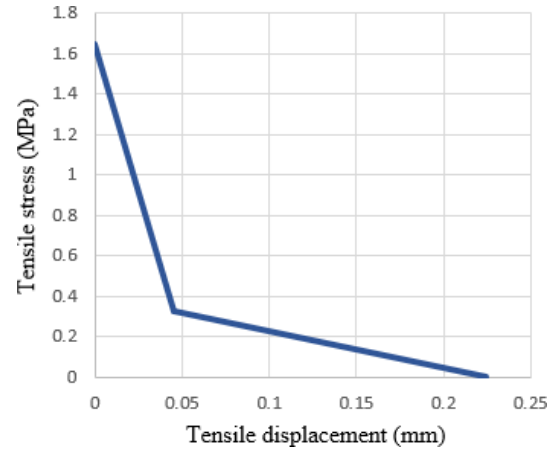
$$f_t = 0.33\sqrt{f'_c}, \tag{10}$$

$$G_f = G_{f0}\left(\left(f'_c + 8\right) \div f_{cmo}\right)^{0.7}, \tag{11}$$

where f_{cmo} = 10 MPa and G_{f0} denotes the base fracture energy depending on the maximum aggregate size of concrete, d_{max}. By assuming that d_{max} = 12 mm the value of the base fracture energy is equal 0.03 N/mm [36].
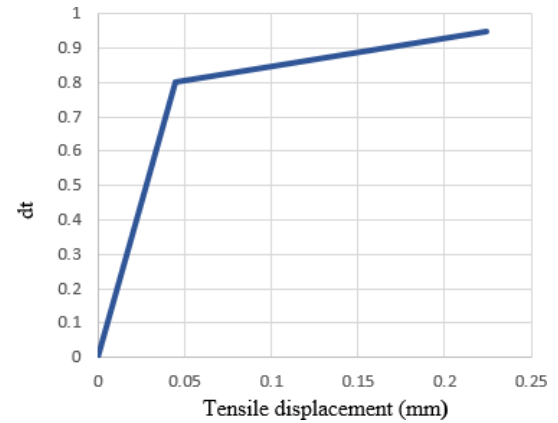
The damage parameter in tension, d_t, was assumed to reach a value of 0.8 when the strength drops by 80%, while its maximum value was chosen as 0.95, corresponding to a 95% reduction in strength. Fig. 7(a) illustrates the tension stress-cracking displacement curve, while Fig. 7(b) depicts the relationship between the tension damage parameter and cracking displacement.

3.3 Reinforcement modelling

In our structural analysis, we have adopted an isotropic modelling approach to characterize both the steel reinforcement and the loading steel plate. Specifically, the steel reinforcement is assumed to exhibit bilinear behaviour, with its mechanical properties obtained directly from experimental test data, as detailed in Table 2 [24]. Simultaneously, the loading steel plate has been represented as a linear material with defined mechanical properties. In this context, a Poisson's ratio of 0.3 and a Young's modulus of 200 GPa have been attributed to the loading steel plate. To visually depict the mechanical response of the steel reinforcement, Fig. 8 provides a clear illustration of its bilinear stress-strain behaviour within our model.

Table 2 Mechanical properties of reinforcing bars

Bar diameter (mm)	14	10
Density (t/mm³)	7.8×10^{-9}	7.8×10^{-9}
Poisson's ratio	0.3	0.3
Young's modulus (GPa)	200	200
Yield strength (MPa)	470	405
Ultimate strength (MPa)	690	670
Yield strain (%)	0.2	0.18
Ultimate strain (%)	15	16

3.4 CFRP modelling

To reinforce the RC-BCJ, and enhance its resistance to shear forces within the joint core, unidirectional fiber sheets were utilized. The CFRP composite material can be modeled either as isotropic [37] or orthotropic [38]. In this investigation, the behavior of CFRP was treated as linearly elastic orthotropic until the point of failure.
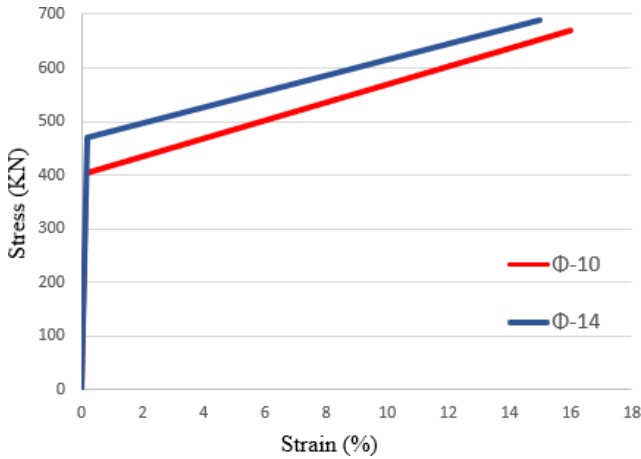
Fig. 8 Bilinear stress-strain diagrams for reinforcing bars

The mechanical properties of orthotropy for the combined CFRP sheets and epoxy adhesive were determined through direct tensile testing performed on two layers of epoxy-coated laminates, as detailed in Table 3 [39].

In order to consider the damage in the CFRP fabric, Hashin's criteria [40] was adopted to detect the evolution of damage in the CFRP fabric. There are four different damage initiation mechanisms in this model, i.e., fiber tension, fiber compression, matrix tension, and matrix compression, and they can be expressed respectively by Eqs. (12)–(15):

1. Fiber in tension ($\sigma_{11} \geq 0$):

$$F_f^t = \left(\frac{\sigma_{11}}{X^T}\right)^2 + \alpha\left(\frac{\tau_{12}}{S^L}\right)^2. \tag{12}$$

2. Fiber in compression ($\sigma_{11} < 0$):

$$F_f^c = \left(\frac{\sigma_{11}}{X^C}\right)^2. \tag{13}$$

3. Matrix in tension ($\sigma_{22} \geq 0$):

$$F_m^t = \left(\frac{\sigma_{22}}{Y^T}\right)^2 + \left(\frac{\tau_{12}}{S^L}\right)^2. \tag{14}$$

Table 3 CFRP Mechanical orthotropic properties [39]

Property	Designation	Value
Young's modulus (GPa)	E_x	46.053
	E_y	3.224
	E_z	3.224
Poisson's ratio	υ_{xy}	0.28
	υ_{xz}	0.28
	υ_{yz}	0.42
Shear modulus (GPa)	G_{xy}	1.259
	G_{xz}	1.259
	G_{yz}	1.135

4. Matrix in compression ($\sigma_{22} < 0$):

$$F_m^c = \left(\frac{\sigma_{22}}{2S^T}\right)^2 + \left[\left(\frac{Y^C}{2S^T}\right)^2 - 1\right]\left(\frac{\sigma_{22}}{Y^C}\right)^2 + \left(\frac{\tau_{12}}{S^L}\right)^2. \tag{15}$$

In Eqs. (12)–(15):
- σ_{11} and σ_{22}: represent normal stresses in the x and y planes, respectively;
- τ_{11} and τ_{22}: denote shear stresses in the x and y planes, respectively;
- X^T: signifies longitudinal tensile strength;
- X^C: indicates longitudinal compressive strength;
- Y^T: represents transverse tensile strength;
- Y^C: stands for transverse compressive strength;
- S^L: refers to longitudinal shear strength;
- S^T: represents transverse shear strength.

4 Analysis verification

The geometric representation of the R2NS model subjected to analysis verification is depicted in Fig. 9. To replicate the boundary conditions of the actual test setup accurately, two reference points were added at the ends of the column. These reference points interact with the column surfaces using the coupling constraint. Then, the boundary conditions were applied to them. The upper surface of the column was constrained in both the X and Z directions ($U_X = U_Z = 0$), simulating a roller support. Conversely, the lower surface was constrained in the X, Y, and Z directions ($U_X = U_Y = U_Z = 0$), representing a pinned support, in accordance with the test conditions. Additionally, the free end of the beam was constrained in the Z direction to prevent any lateral movement. In order to mirror the experimental loading conditions, two distinct load steps were implemented. The first step involved the application of a consistent axial pressure of 2.8 MPa to the upper surface of the column, which was maintained throughout the analysis. This corresponds to an axial force of 175 kN. Subsequently, in the second step, the beam load was introduced by means of controlled displacement at a designated reference point situated at the center of the steel loading plate. Notably, a purely monotonic displacement was applied at the beam end, thereby simplifying the analysis and circumventing the intricate calculations associated with cyclic loading analysis. Importantly, this approach has been employed in various prior numerical investigations conducted on RC-BCJs for the purpose of analysis validation [37, 41–43].

The envelopes of the experimental hysteresis curves were computed and subsequently juxtaposed with the
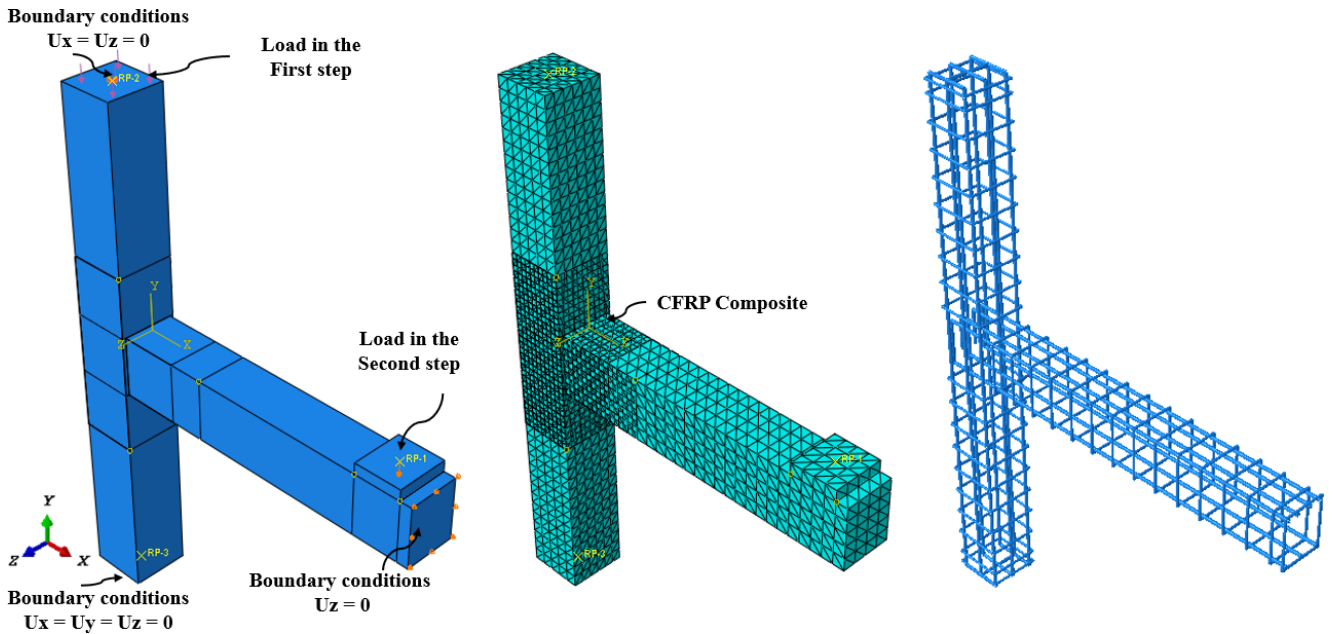
Fig. 9 Details and geometric representation of R2NS model

numerical beam load-displacement curves, thereby facilitating the evaluation of the analysis's precision and credibility. Fig. 10, illustrates the comparison between the beam load-displacement curve subjected to experimental testing and the numerical models. The predicted peak loads, as derived from the numerical analysis, for the NS and R2NS specimens were 39.01 KN and 49.15 KN, respectively. In contrast, the corresponding experimental peak loads were 38.00 KN and 50.46 KN. On the whole, the load-displacement curve produced by the finite element analysis FEA demonstrated a commendable agreement with the experimental data. As depicted in Fig. 10, the numerical initial stiffness of the NS and R2NS specimens was found to be marginally higher than that observed experimentally. This slight variation in the results can be

deemed acceptable when accounting for potential minor disparities between the input and measured properties of the test parameters, the idealized bond assumption between reinforcement and concrete, or any potential material irregularities encountered during the experimental tests.

The crack patterns for both NS and R2NS specimens, as derived from numerical simulations, are on display in Fig. 11. This illustration portrays the plastic strain distributions at peak loads and facilitates a comprehensive comparative analysis with the corresponding results obtained from experimental testing. For the FE outcomes of the bare NS specimen, it is observed that the flexural cracks initially appear in the beam, and then they propagate into the joint core area, where shear cracks begin to develop. As the loading process continues, the number of shear

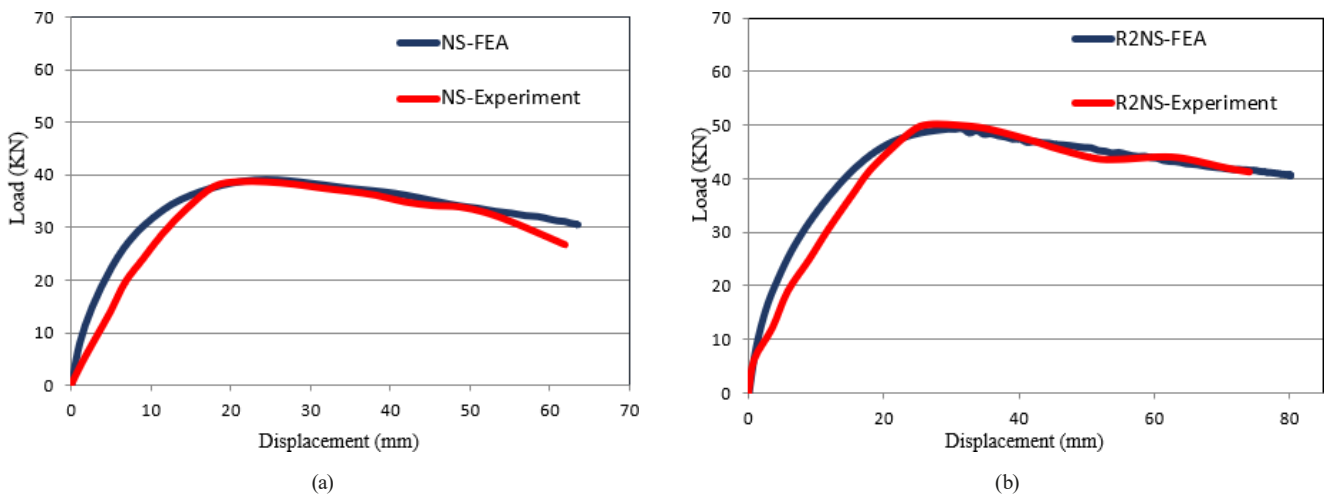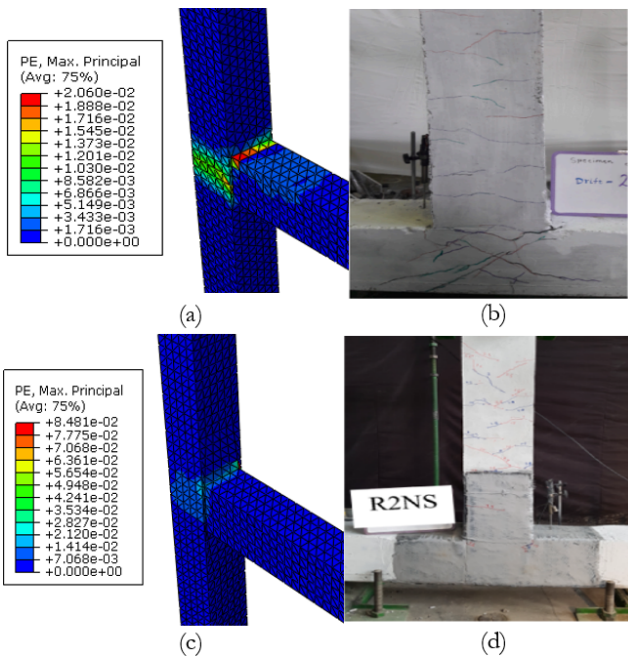(a)   (b)

Fig. 10 Comparison of the beam load-displacement curves: numerical analysis vs. experimental test; (a) NS specimen; (b) R2NS specimen

Fig. 11 Failure modes of the tested specimens; (a) numerical crack pattern for NS; (b) experimental crack pattern for NS; (c) numerical crack pattern for R2NS; (d) experimental crack pattern for R2NS

diagonal cracks increases. Eventually, the bare NS specimen fails in a brittle shear failure mode due to the absence of horizontal stirrups in the joint core region. This observation aligns with the experimental results. In contrast, the R2NS model exhibits a somewhat distinct behavior. Prior to reaching the peak load, cracks manifest solely within the beam, in the form of flexural cracks within the sections retrofitted with CFRP sheets. Upon reaching the peak load, a few shear cracks emerge in the joint core area, due to the initiation of damage within the CFRP material. In the experimental phase, and during the latter stages of loading, distinct occurrences are noted, the detachment of a portion of the concrete cover with the CFRP sheets and the separation of the CFRP composite from the concrete surface began, both occurring specifically on the beam. It is noteworthy that this observation does not manifest in the numerical model, as it relies on the assumption of a perfect bond between the CFRP material and the concrete substrate. Nevertheless, the load-displacement curves obtained from the numerical simulations closely mirror the experimental results, especially within the nonlinear phase. Thus, the numerical models demonstrated a level of agreement that was deemed acceptable.

5 Parametric study

Building on the validated accuracy of the developed FE model, a parametric analysis was conducted to assess the influence of key parameters on the performance of the retrofitting technique explored in this study. The parameters examined include the column axial load ratio, beam longitudinal reinforcement ratio and joint aspect ratio. This analysis aims to deepen understanding of how these factors affect the overall effectiveness of the retrofit method.

5.1 Effect of column axial load

Section 5.1 of the study examines the effect of the column axial load ratio on the behavior of retrofitted BCJs through finite element analysis. Four distinct axial load levels $\left(0,\ 0.1A_g f_c',\ 0.2A_g f_c',\ \text{and}\ 0.3A_g f_c'\right)$ were investigated for joints both with and without CFRP composites to assess the retrofit's influence on strength and ductility. These axial load levels were selected due to their tendency to induce shear failure in un-retrofitted joints. Fig. 12 illustrates the lateral force versus horizontal displacement behavior under varying axial load levels, while Table 4 provides a comprehensive summary of the results, including peak load (P_u), displacement at peak (Δ_u) and the obtained numerical joint shear strength (v_j) for each axial load ratio.

Analysis of Fig. 12 and Table 4 reveals notable trends. Specifically, in un-retrofitted specimens, the lateral force increased by approximately 25% as the axial load ratio transitioned from $0A_g f_c'$ to $0.3A_g f_c'$. This significant increase suggests that the axial load plays a crucial role in enhancing the shear strength of the joint. In contrast, retrofitted specimens showed a smaller increase of around 16% over the same range of axial load. This smaller increase can be attributed to the additional confinement provided by the CFRP material, which improves the joint shear strength and mitigates the impact of the column axial load on the lateral force.

However, the peak load showed percentage increases of 26.64%, 25.99%, 22.49%, and 16.63% for retrofitted joints compared to control joints at axial load levels of 0, $0.1A_g f_c'$, $0.2A_g f_c'$, and $0.3A_g f_c'$, respectively. These results indicate that while CFRP significantly enhances the shear strength of the joint, its relative contribution decreases as the column axial load increases. The higher column axial loads enhance the inherent shear strength of the joint panel, reducing the incremental benefit provided by CFRP retrofitting.

The most significant improvement in peak load (26.64%) was observed in the absence of axial load. This suggests that the CFRP composite exhibits full participation in reinforcing the joint when there is no axial load. Under these conditions, the CFRP can fully engage in resisting the shear forces without being supplemented by the additional
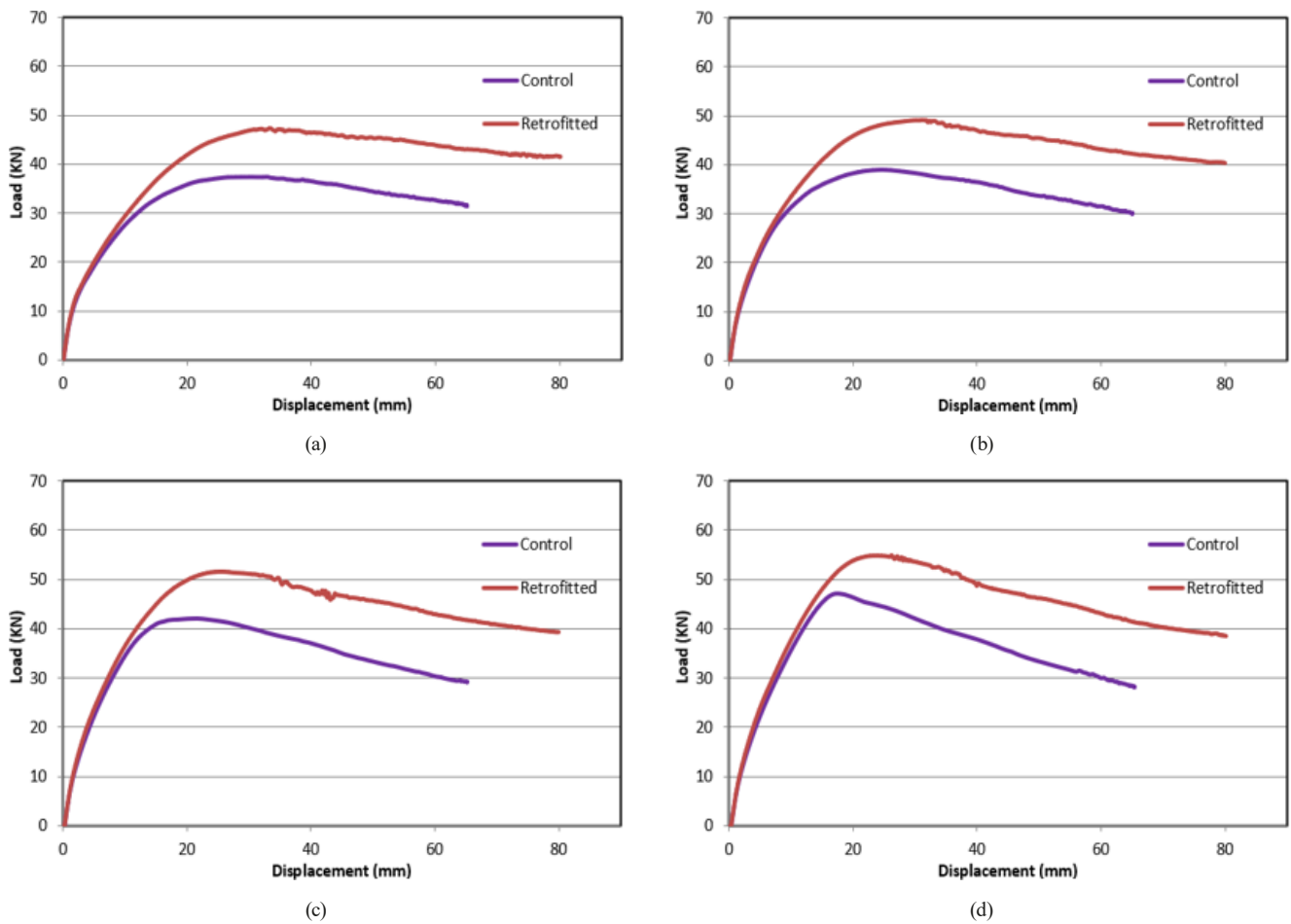
Fig. 12 Effect of column axial load ratio on the load-displacement curves; (a) $N = 0.0$; (b) $N = 0.1$; (c) $N = 0.2$; (d) $N = 0.3$

Table 4 Output results for different column axial load ratio

Ratios	Peak load (P_u) (KN)		Displacement at peak (Δ_u) (mm)		v_j (Mpa)		Gain in P_u %
	Control	Retrofitted	Control	Retrofitted	Control	Retrofitted	
0.0	37.39	47.35	30.32	33.42	4.27	5.41	26.24
0.1	39.01	49.15	24.85	31.08	4.46	5.62	25.99
0.2	42.06	51.52	21.63	25.41	4.80	5.89	22.49
0.3	47.00	54.82	17.05	23.52	5.37	6.26	16.63

shear strength from the axial load. The extensive involvement of the CFRP composite in retrofitting was particularly evident in joints with lower initial shear strengths, where it played a critical role in confining the panel zone against the shear forces induced by lateral loads. This highlights the importance of CFRP in retrofitting applications where the existing shear capacity is insufficient.

The reduced percentage increase in peak load for retrofitted joints at higher axial loads (16.63% at $0.3 A_g f_c'$) indicates diminishing returns from CFRP retrofitting as the axial load increases. As the joint's shear strength is already enhanced by the higher axial load, the additional confinement and tensile strength provided by the CFRP become less critical.

In Fig. 13, the tensile damage contours for retrofitted joints under various axial loads are depicted. The illustration highlights how an escalation in column axial load redistributes tensile damage from the joint area to the beam. Additionally, it confirms that higher axial load levels effectively confine the area of joints from developing diagonal shear cracks. Notably, in the absence of column axial load Fig. 13(a), severe diagonal shear cracks are observed, indicating the full engagement of the CFRP composite in reinforcing the joint area under this condition.
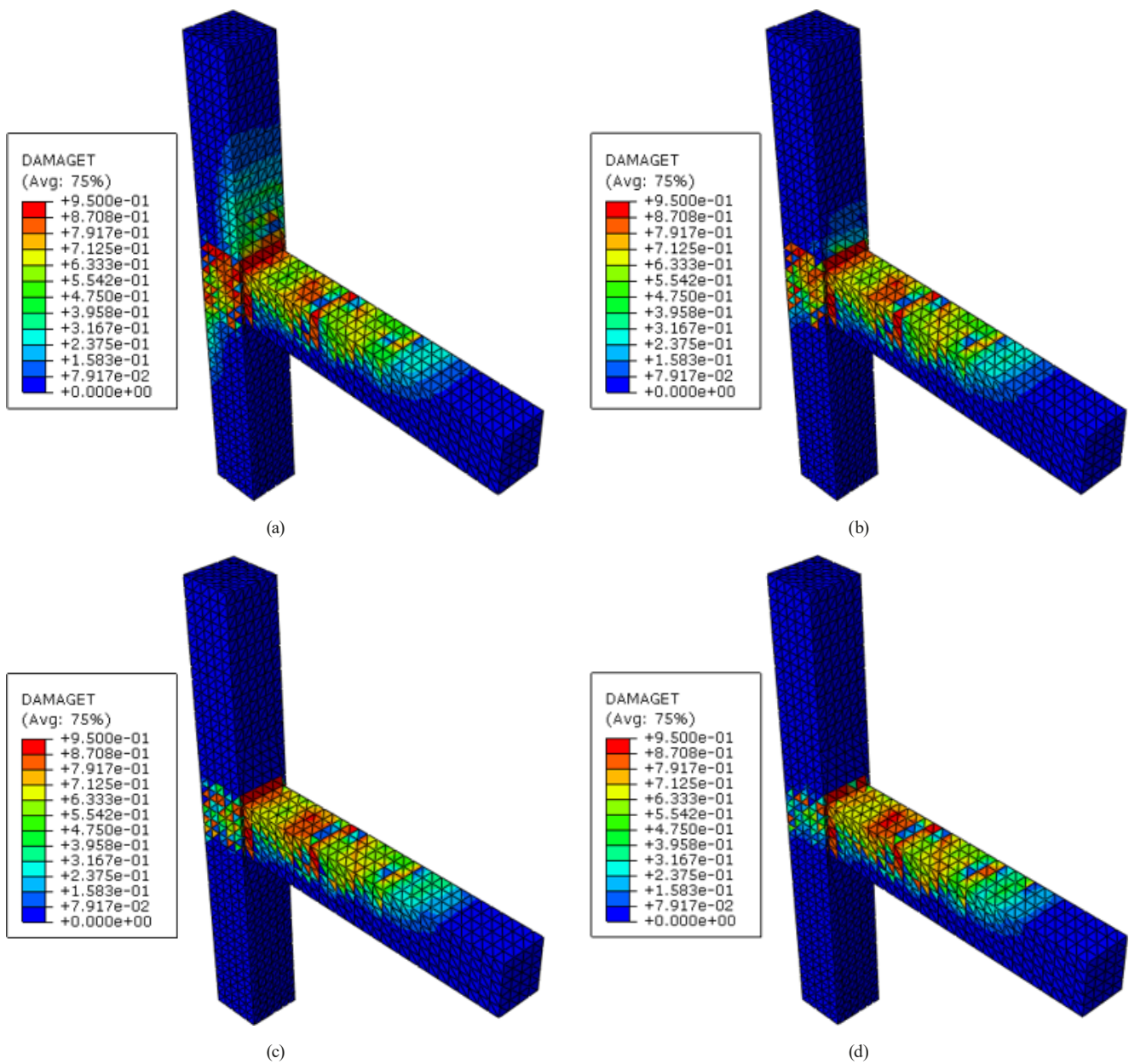
(a)

(b)

(c)

(d)

Fig. 13 Effect of column axial load ratio on the tensile damage of joints at peak load; (a) $N/(A_g \times f_c') = 0$; (b) $N/(A_g \times f_c') = 0.1$; (c) $N/(A_g \times f_c') = 0.2$; (d) $N/(A_g \times f_c') = 0.3$

5.2 Effect of beam longitudinal reinforcement ratio

The investigation involved simulating and analyzing various longitudinal reinforcement ratios in beams: 0.99%, 1.44%, 1.95%, and 2.55%. The reinforcement ratios were adjusted by maintaining the same number of rebars with consistent mechanical properties while varying their diameters. Fig. 14 presents the resulting load-displacement curves for specimens with and without CFRP composites. Additionally, Table 5 summarizes the key output parameters, including peak load (P_u) and displacement at peak load (Δ_u) and the obtained numerical joint shear strength (v_j) for each reinforcement ratio.

The analysis of Fig. 14 and Table 5 reveals a significant improvement in the load-carrying capacity of joints without CFRP composites when increasing the beam reinforcement ratio from 0.99% to 2.55%, resulting in approximately a 46% increase. This enhancement is attributed to the increased beam reinforcement, which improves the beam's ability to resist flexural loads and leads to a notable increase in load-carrying capacity, especially where beam flexural failure was observed at the lowest reinforcement ratios.

In contrast, joints retrofitted with CFRP composites exhibited a slightly lower increase in load-carrying capacity, about 36%. This suggests that while both scenarios
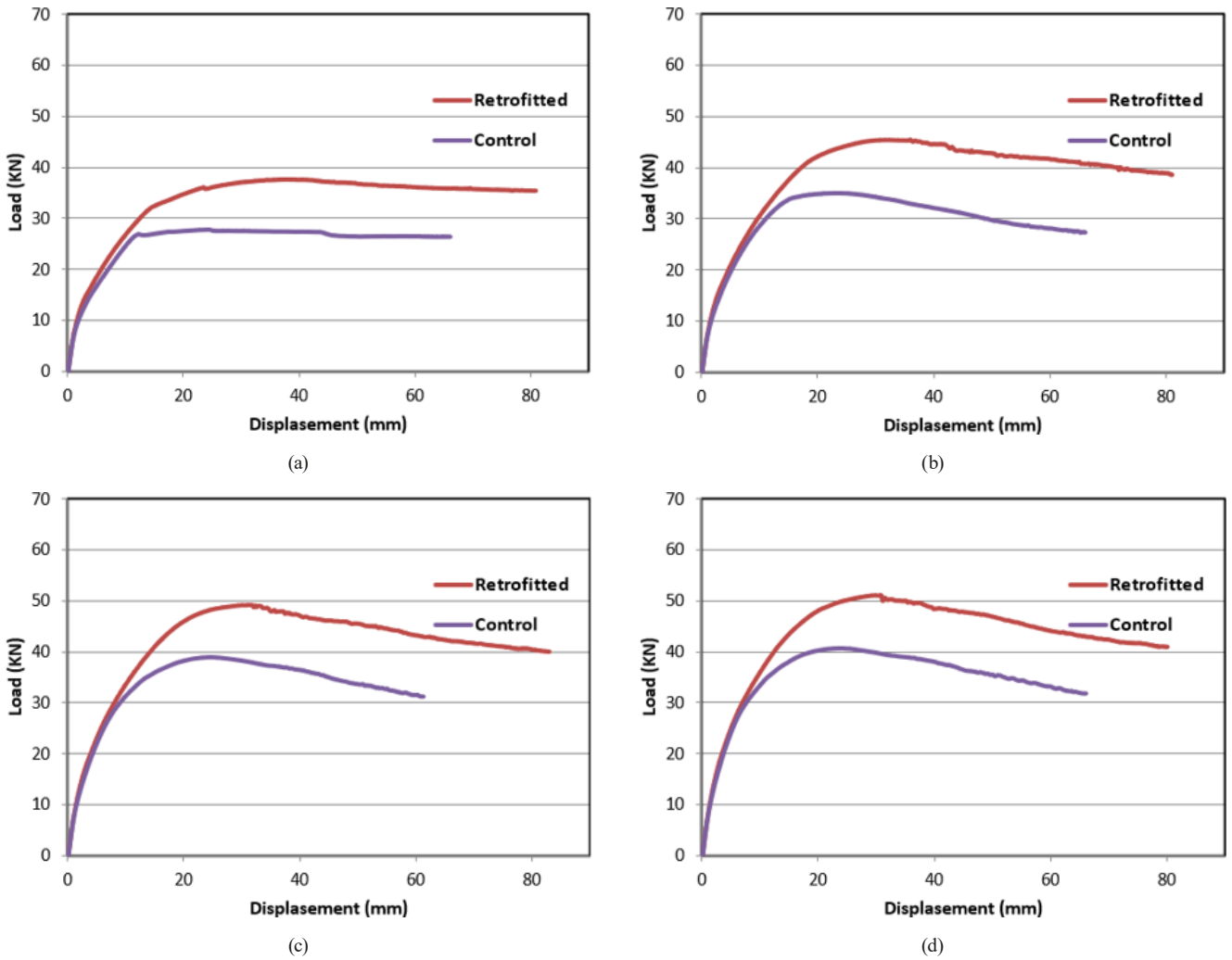
Fig. 14 Effect of beam longitudinal reinforcement ratio on the load-displacement curves; (a) 0.99%; (b) 1.44%; (c) 1.95%; (d) 2.55%

Table 5 Output results for different beam reinforcements ratio

Ratios	Peak load (P_u) (KN)		Displacement at peak (Δ_u) (mm)		v_j (Mpa)		Gain in P_u %
	Control	Retrofitted	Control	Retrofitted	Control	Retrofitted	
0.99	27.87	37.54	24.51	38.03	3.18	4.29	34.69
1.44	35.01	45.33	23.62	32.07	4.00	5.18	29.47
1.95	39.01	49.15	24.85	31.07	4.46	5.62	25.99
2.55	40.70	51.03	24.06	29.60	4.65	5.83	25.38

showed enhancements, the impact of CFRP retrofitting on load-bearing capacity was marginally less pronounced compared to joints without such reinforcement. The CFRP wraps around the beam enhance the beam's flexural capacity by providing additional confinement. However, this increased capacity also results in a greater load being transferred to the joint as shear force, leading to a reduced relative increase in load-carrying capacity. This shift in failure mode from beam flexural failure to joint shear failure due to the increased beam reinforcement ratio explains the smaller increase observed in CFRP-retrofitted joints.

Moreover, the peak load exhibited a percentage increase of 34.96%, 29.47%, 25.99%, and 25.38% for retrofitted joints compared to control joints, corresponding to beam reinforcement ratios of 0.99%, 1.95%, 35.01%, and 2.55%, respectively. Notably, the lowest percentage increase (25.38% and 25.99%) was observed for the highest ratios (2.55% and 1.95%). This phenomenon can be attributed to the observed shear failure in the control joints, where CFRP composites serve as shear retrofitting materials and play a crucial role in confining the panel zone from severe shear cracks.

Conversely, the highest improvement in peak load, 34.69%, was observed for a beam longitudinal ratio of 0.99%, where beam flexural failure was observed in the control joint instead of joint shear failure. This was confirmed by the ductility observed in the load-displacement curve, as shown in Fig. 14(a). In this case, the CFRP composites functioned as beam flexural retrofitting material, playing a crucial role in confining the beam from flexural failure.

5.3 Effect of joint aspect ratio

To investigate the impact of the joint aspect ratio ($\eta = h_b/h_c$) on the performance of retrofitted joints, numerical models were analyzed for various aspect ratios: $\eta = 1$ ($h_b = 250$ mm), $\eta = 1.2$ ($h_b = 300$ mm), $\eta = 1.4$ ($h_b = 350$ mm), and $\eta = 1.6$ ($h_b = 400$ mm), where h_b and h_c represent the beam and column depths, respectively. The performance of the joints was evaluated by incorporating joint transverse reinforcement in the joint region of all models, with two-leg horizontal stirrups spaced at 50 mm intervals, complying with ACI 318-19 [33] requirements for maximum stirrup spacing. For consistency in comparing different joint aspect ratios, only three layers of U-jacketing were applied around the joint area in all models.

The load-displacement curves for the analyzed models are presented in Fig. 15, with the corresponding output results summarized in Table 6. The data indicate that for a joint aspect ratio of $\eta = 1$, the retrofitted joint shows no significant improvement in peak load compared to the control specimen, as the joint shear capacity had already been enhanced by the provision of horizontal stirrups. However, retrofitted joints exhibit only marginal gains in peak load of 3.09%, 3.43%, and 6.68% for joint aspect ratios of $\eta = 1.2$, $\eta = 1.4$ and $\eta = 1.6$, respectively. These gains can be attributed to the influence of the joint aspect ratio on the joint's resistance mechanism. As the joint aspect ratio increases, the shear strength of the joint decreases, allowing the CFRP reinforcement to contribute more effectively to the joint's performance. The stress distribution in the CFRP composites, depicted in Fig. 16, demonstrates a significant increase in induced stress intensity as the joint aspect ratio rises. This indicates that the CFRP reinforcement becomes more effective in joints with higher aspect
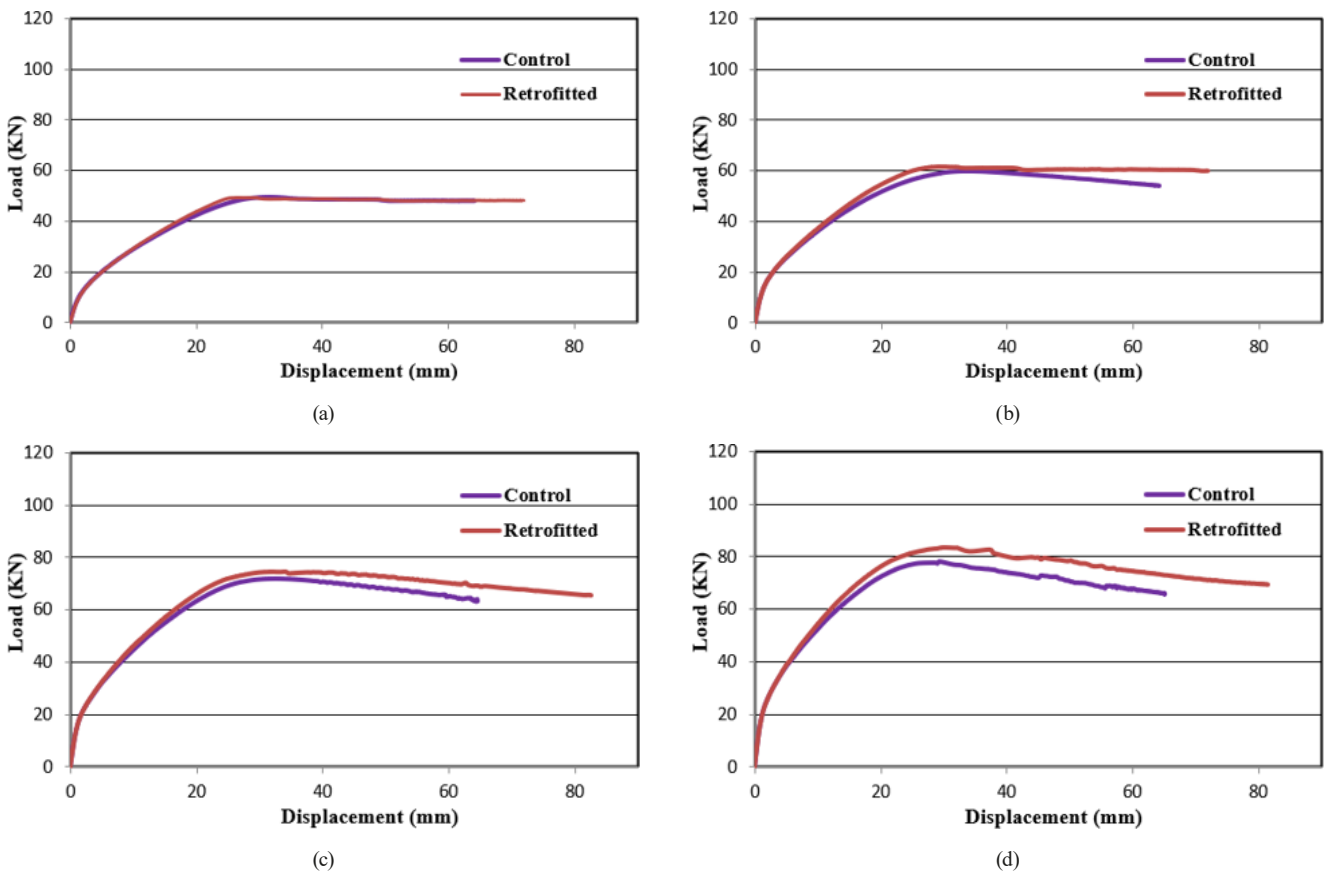

Fig. 15 Effect of joint aspect ratio on the load-displacement curves; (a) $\eta = 1.0$; (b) $\eta = 1.2$; (c) $\eta = 1.4$; (d) $\eta = 1.6$

Table 6 Output results for different joint aspect ratio

Models	Beam depth (mm)	η	Peak load (Pu) (KN)		Displacement at peak (Δu) (mm)		vj (Mpa)		Gain in Pu (%)
			Control	Retrofitted	Control	Retrofitted	Control	Retrofitted	
With horizontal stirrups spaced at 50 mm	250	1.0	49.30	49.08	31.72	26.21	5.64	5.61	No increase
	300	1.2	59.71	61.56	33.12	29.21	5.45	5.62	3.09
	350	1.4	72.05	74.52	32.65	33.80	5.44	5.62	3.43
	400	1.6	78.38	83.62	31.89	29.96	5.00	5.33	6.68
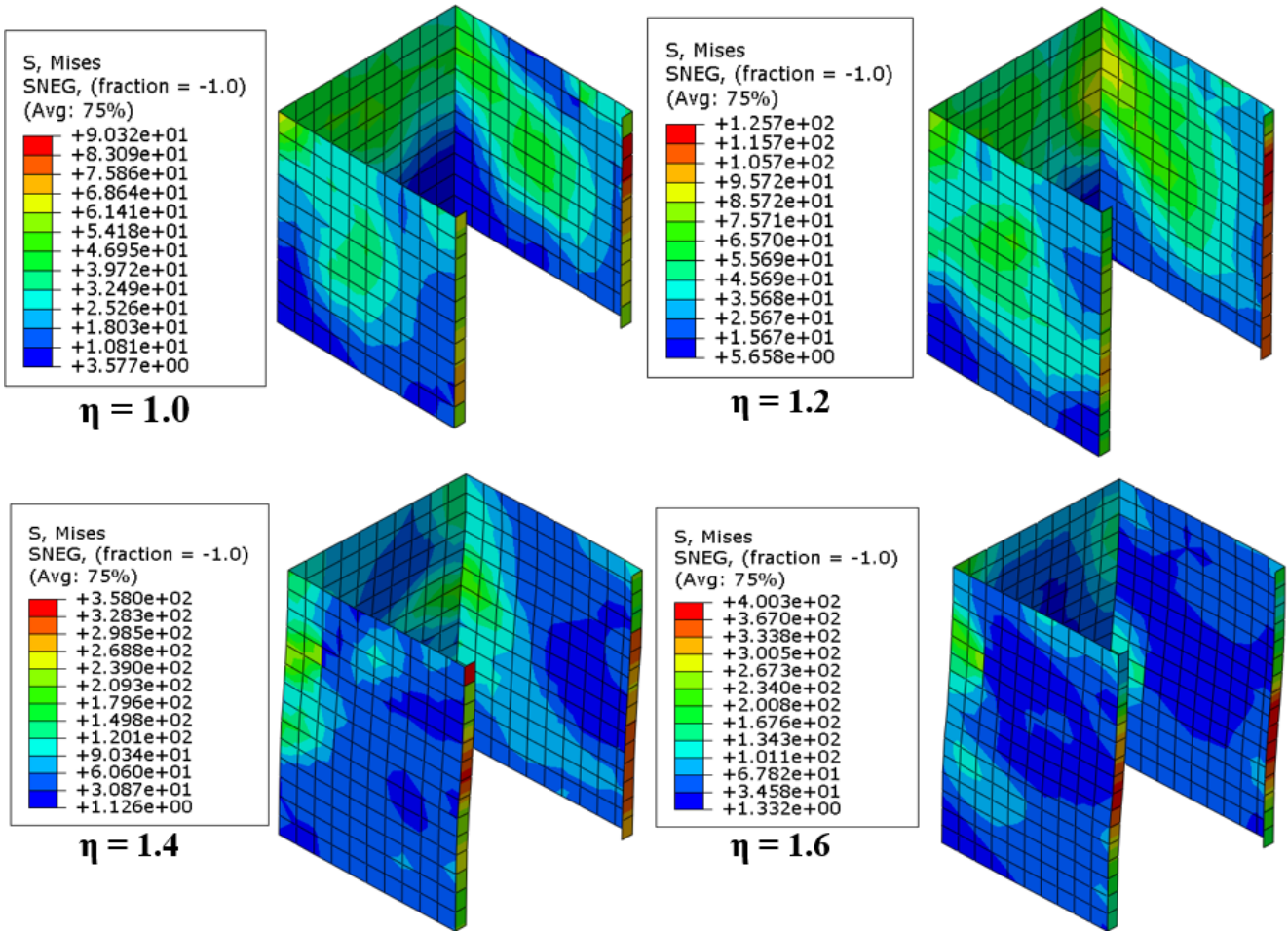
Fig. 16 Stress distribution in CFRP composites under varying joint aspect ratios

ratios. However, Fig. 16 also shows a noticeable trend of increasing stress concentrations with higher joint aspect ratios. This trend suggests that the joint's ability to evenly distribute loads decreases as the aspect ratio increases. Which allow the CFRP to work more effectively.

6 Discussion
The numerical investigation conducted in this study reveals significant insights regarding the effectiveness of CFRP composites for retrofitting seismically vulnerable BCJs. The results demonstrate that CFRP retrofitting markedly enhances both shear strength and ductility, particularly

when no axial load is applied. This underscores the composite's critical role in confining the joint area and improving overall load-carrying capacity. However, as axial loads increase, the relative contribution of CFRP diminishes, indicating that while CFRP remains beneficial, its impact is more pronounced under lower axial load conditions.

Furthermore, increasing the beam longitudinal reinforcement ratio results in substantial improvements in the load-carrying capacity of un-retrofitted joints, whereas the gains in retrofitted joints are comparatively lower. This suggests that existing reinforcement conditions significantly influence the effectiveness of CFRP. The findings also

highlight that higher joint aspect ratios tend to decrease shear capacity, thereby allowing CFRP composites to engage more effectively in enhancing joint performance. Nonetheless, this study acknowledges certain limitations, including a limited range of parameters investigated. Future research should prioritize experimental work that explores these parameters and conduct analytical investigations to further refine the understanding of CFRP retrofitting.

7 Conclusions

This paper presents the FEA to assess the behavior of RC exterior BCJs retrofitted with CFRP composites using the GM. Two experimental specimens were simulated and analyzed for validation purposes. The CDP model in ABAQUS was used to simulate concrete behavior. The interaction between the CFRP composites and the concrete substrate was modeled as a perfect bond to simulate the strong adhesion achieved through the grooving technique. FEA predictions were compared with experimental results, and a parametric investigation was conducted to explore the influence of several parameters on the performance of retrofitted joints. The key conclusions drawn from this research are as follows:

1. The proposed numerical model successfully predicted the load-displacement envelope curves, peak loads, and failure modes with an acceptable degree of accuracy, as demonstrated by comparison with experimental results.

2. Increasing the column axial load ratio significantly enhances the joint shear strength, thereby reducing the incremental benefit provided by CFRP retrofitting.

3. The joint without axial load in the column exhibited a significant improvement in peak load, highlighting the effectiveness of CFRP retrofitting in this scenario.

4. At lower beam reinforcement ratios, reinforcing the beam near the column becomes essential when the failure mode shifts from joint shear failure to beam flexural failure.

5. Retrofitted joints with transverse reinforcement in the joint region exhibited only marginal gains in peak load compared to the control specimens, indicating limited effectiveness of CFRP retrofitting in such cases.

6. As the joint aspect ratio increases, the shear capacity of the joints decreases. This reduction in shear strength allows the CFRP retrofit to contribute more effectively, particularly in joints with higher aspect ratios.

References

[1] Wang, G.-L., Dai, J.-G., Bai, Y.-L. "Seismic retrofit of exterior RC beam-column joints with bonded CFRP reinforcement: An experimental study", Composite Structures, 224, 111018, 2019.
https://doi.org/10.1016/j.compstruct.2019.111018

[2] Najafgholipour, M. A., Arabi, A. R. "A nonlinear model to apply beam-column joint shear failure in analysis of RC moment resisting frames", Structures, 22, pp. 13–27, 2019.
https://doi.org/10.1016/j.istruc.2019.07.011

[3] Engindeniz, M., Kahn, L. F., Zureick, A.-H. "Repair and Strengthening of Reinforced Concrete Beam-Column Joints: State of the Art", ACI Structural Journal, 102(2), pp. 187–197, 2005.
https://doi.org/10.14359/14269

[4] Khan, M. I., Al-Osta, M. A., Ahmad, S., Rahman, M. K. "Seismic behavior of beam-column joints strengthened with ultra-high performance fiber reinforced concrete", Composite Structures, 200, pp. 103–119, 2018.
https://doi.org/10.1016/j.compstruct.2018.05.080

[5] Campione, G., Cavaleri, L., Papia, M. "Flexural response of external R.C. beam-column joints externally strengthened with steel cages", Engineering Structures, 104, pp. 51–64, 2015.
https://doi.org/10.1016/j.engstruct.2015.09.009

[6] Yen, J. Y. R., Chien, H. K. "Steel plates rehabilitated RC beam-column joints subjected to vertical cyclic loads", Construction and Building Materials, 24(3), pp. 332–339, 2010.
https://doi.org/10.1016/j.conbuildmat.2009.08.029

[7] Li, B., Lam, E. S.-S., Wu, B., Wang, Y.-Y. "Experimental investigation on reinforced concrete interior beam-column joints rehabilitated by ferrocement jackets", Engineering Structures, 56, pp. 897–909, 2015.
https://doi.org/10.1016/j.engstruct.2013.05.038

[8] Shaaban, I. G., Seoud, O. A. "Experimental behavior of full-scale exterior beam-column space joints retrofitted by ferrocement layers under cyclic loading", Case Studies in Construction Materials, 8, pp. 61–78, 2018.
https://doi.org/10.1016/j.cscm.2017.11.002

[9] Rizkalla, S., Hassan, T., Hassan, N. "Design recommendations for the use of FRP for reinforcement and strengthening of concrete structures", Progress in Structural Engineering and Materials, 5(1), pp. 16–28, 2003.
https://doi.org/10.1002/pse.139

[10] Le-Trung, K., Lee, K., Lee, J., Lee, D. H., Woo, S. "Experimental study of RC beam–column joints strengthened using CFRP composites", Composites Part B: Engineering, 41(1), pp. 76–85, 2010.
https://doi.org/10.1016/j.compositesb.2009.06.005

[11] Ghobarah, A., Said, A. "Shear strengthening of beam-column joints", Engineering Structures, 24(7), pp. 881–888, 2002.
https://doi.org/10.1016/S0141-0296(02)00026-3

[12] Tsonos, A. G. "Effectiveness of CFRP-jackets and RC-jackets in post-earthquake and pre-earthquake retrofitting of beam-column subassemblages", Engineering Structures, 30(3), pp. 777–793, 2008.
https://doi.org/10.1016/j.engstruct.2007.05.008

[13] Sezen, H. "Repair and Strengthening of Reinforced Concrete Beam-Column Joints with Fiber-Reinforced Polymer Composites", Journal of Composites for Construction, 16(5), pp. 499–506, 2012.
https://doi.org/10.1061/(ASCE)CC.1943-5614.0000290

[14] Mahmoud, M. H., Afefy, H. M., Kassem, N. M., Fawzy, T. M. "Strengthening of defected beam–column joints using CFRP", Journal of Advanced Research, 5(1), pp. 67–77, 2014.
https://doi.org/10.1016/j.jare.2012.11.007

[15] El-Amoury, T., Ghobarah, A. "Seismic rehabilitation of beam–column joint using GFRP sheets", Engineering Structures, 24(11), pp. 1397–1407, 2002.
https://doi.org/10.1016/S0141-0296(02)00081-0

[16] Granata, P. J., Parvin, A. "An experimental study on Kevlar strengthening of beam-column connections", Composites Structures, 53(2), pp. 163–171, 2001.
https://doi.org/10.1016/S0263-8223(00)00187-2

[17] Ong, C.-B., Chin, C.-L., Ma, C.-K., Tan, J.-Y., Awang, A. Z., Omar, W. "Seismic retrofit of reinforced concrete beam-column joints using various confinement techniques: A review", Structures, 42, pp. 221–243, 2022.
https://doi.org/10.1016/j.istruc.2022.05.114

[18] Jalaeian Zaferani, M., Shariatmadar, H. "Repair and retrofitting of external RC beam-to-column joints using the hybrid NSM+EBR method", Engineering Structures, 263, 114370, 2022.
https://doi.org/10.1016/j.engstruct.2022.114370

[19] Mostofinejad, D., Hajrasouliha, M. "Shear Retrofitting of Corner 3D-Reinforced Concrete Beam-Column Joints Using Externally Bonded CFRP Reinforcement on Grooves", Journal of Composites for Construction, 22(5), 04018037, 2018.
https://doi.org/10.1061/(ASCE)CC.1943-5614.0000862

[20] Mostofinejad, D., Akhlaghi, A. "Experimental Investigation of the Efficacy of EBROG Method in Seismic Rehabilitation of Deficient Reinforced Concrete Beam–Column Joints Using CFRP Sheets", Journal of Composites for Construction, 21(4), 04016116, 2017.
https://doi.org/10.1061/(ASCE)CC.1943-5614.0000781

[21] Mostofinejad, D., Hajrasouliha, M. "3D beam–column corner joints retrofitted with X-shaped FRP sheets attached via the EBROG technique", Engineering Structures, 183, pp. 987–998, 2019.
https://doi.org/10.1016/j.engstruct.2019.01.038

[22] Ilia, E., Mostofinejad, D. "Seismic retrofit of reinforced concrete strong beam–weak column joints using EBROG method combined with CFRP anchorage system", Engineering Structures, 194, pp. 300–319, 2019.
https://doi.org/10.1016/j.engstruct.2019.05.070

[23] Ilia, E., Mostofinejad, D., Moghaddas, A. "Cyclic behavior of strong beam–weak column joints strengthened with different configurations of CFRP sheets", Archives of Civil and Mechanical Engineering, 20(2), 31, 2020.
https://doi.org/10.1007/s43452-020-0015-7

[24] Davodikia, B., Saghafi, M. H., Golafshar, A. "Experimental investigation of grooving method in seismic retrofit of beam-column external joints without seismic details using CFRP sheets", Structures, 34, pp. 4423–4434, 2021.
https://doi.org/10.1016/j.istruc.2021.10.023

[25] Nie, X. F., Zhang, S. S., Chen, G. M., Yu, T. "Strengthening of RC beams with rectangular web openings using externally bonded FRP: Numerical simulation", Composites Structures, 248, 112552, 2020.
https://doi.org/10.1016/j.compstruct.2020.112552

[26] Behnam, H., Kuang, J. S., Samali, B. "Parametric finite element analysis of RC wide beam-column connections", Computers & Structures, 205, pp. 28–44, 2018.
https://doi.org/10.1016/j.compstruc.2018.04.004

[27] Dadmand, B., Pourbaba, M., Riahi, R. "Experimental and Numerical Investigation of Different Types of Jacketing Effect on Retrofitting RC Short Columns Using ECC Concrete", Periodica Polytechnica Civil Engineering, 66(2), pp. 603–613, 2022.
https://doi.org/10.3311/PPci.19114

[28] Abdesselam, A., Merdas, A., Fiorio, B., Chikh, N.-D. "Experimental and Numerical Study on RC Beams Strengthened by NSM Using CFRP Reinforcements", Periodica Polytechnica Civil Engineering, 67(4), pp. 1214–1233, 2023.
https://doi.org/10.3311/PPci.21309

[29] Simulia "Abaqus 6.14: Abaqus Analysis User's Guide: Volume V: Prescribed Conditions, Constraints & Interactions", Dassault Systèmes Simulia Corp., Providence, RI, USA, 2014.

[30] El-Naqeeb, M. H., Hassanli, R., Zhuge, Y., Ma, X., Manalo, A. "Numerical investigation on the behaviour of socket connections in GFRP-reinforced precast concrete", Engineering Structures, 303(3), 117489, 2024.
https://doi.org/10.1016/j.engstruct.2024.117489

[31] El-Naqeeb, M. H., El-Metwally, S. E., Abdelwahed, B. S. "Performance of exterior beam-column connections with innovative bar anchorage schemes: Numerical investigation", Structures, 44, pp. 534–547, 2022.
https://doi.org/10.1016/j.istruc.2022.08.034

[32] Saenz, L. P. "Discussion of "Equation for the stress-strain curve of concrete" by Desayi and Krishnan", ACI Journal, 61(9), pp. 1229–1235, 1964.

[33] ACI "ACI 318-19 Building Code Requirements for Structural Concrete and Commentary", American Concrete Institute, Farmington Hills, MI, USA, 2019.

[34] Jankowiak, T., Łodygowski, T. "Identification of Parameters of Concrete Damage Plasticity Constitutive Model", Foundations of Civil and Environmental Engineering, 6(1), pp. 53–69, 2005.

[35] Hillerborg, A., Modéer, M., Petersson, P.-E. "Analysis of Crack Formation and Crack Growth in Concrete by Means of Fracture Mechanics and Finite Elements", Cement and Concrete Research, 6(6), pp. 773–781, 1976.
https://doi.org/10.1016/0008-8846(76)90007-7

[36] Comite Euro-International Du Beton "CEB-FIP-Model Code 90", Thomas Telford Ltd., 1993. ISBN 978-0-7277-1696-5

[37] Saad, A. G., Sakr, M. A., El-korany, T. M. "The shear strength of existing non-seismic RC beam-column joints strengthened with CFRP Sheets: Numerical and analytical study", Engineering Structures, 291, 116497, 2023.
https://doi.org/10.1016/j.engstruct.2023.116497

[38] Abu Tahnat, Y. B., Dwaikat, M. M. S., Samaaneh, M. A. "Effect of using CFRP wraps on the strength and ductility behaviors of exterior reinforced concrete joint", Composite Structures, 201, pp. 721–739, 2018.
https://doi.org/10.1016/j.compstruct.2018.06.082

[39] Choobbor, S. S., Hawileh, R. A., Abu-Obeidah, A., Abdalla, J. A. "Performance of hybrid carbon and basalt FRP sheets in strengthening concrete beams in flexure", Composite Structures, 227, 111337, 2019.
https://doi.org/10.1016/j.compstruct.2019.111337

[40] Hashin, Z. "Failure Criteria for Unidirectional Fiber Composites", Journal of Applied Mechanics, 47(2), pp. 329–334, 1980.
https://doi.org/10.1115/1.3153664

[41] El-Naqeeb, M. H., Abdelwahed, B. S., El-Metwally, S. E. "Numerical investigation of RC exterior beam-column connection with different joint reinforcement detailing", Structures, 38, pp. 1570–1581, 2022.
https://doi.org/10.1016/j.istruc.2022.03.014

[42] Bahraq, A. A., Al-Osta, M. A., Khan, M. I., Ahmad, S. "Numerical and analytical modeling of seismic behavior of beam-column joints retrofitted with ultra-high performance fiber reinforced concrete", Structures, 32, pp. 1986–2003, 2021.
https://doi.org/10.1016/j.istruc.2021.04.004

[43] El-Naqeeb, M. H., Abdelwahed, B. S. "Nonlinear finite element investigations on different configurations of exterior beam-column connections with different concrete strengths in column and floor", Structures, 50, pp. 1809–1826, 2023.
https://doi.org/10.1016/j.istruc.2023.02.122